Microstructure, transport, and acoustic properties of open-cell foam samples: Experiments and three-dimensional numerical simulations

Camille Perrot,[1,2,a] Fabien Chevillotte,[3] Minh Tan Hoang,[1,4] Guy Bonnet,[1] François-Xavier Bécot,[3] Laurent Gautron,[5] and Arnaud Duval[4]

[1]*Université Paris-Est, Laboratoire Modélisation et Simulation Multi Echelle, MSME UMR 8208 CNRS, 5 bd Descartes, Marne-la-Vallée 77454, France*
[2]*Université de Sherbrooke, Department of Mechanical Engineering, Québec J1K 2R1, Canada*
[3]*Matelys - Acoustique & Vibrations, 1 rue Baumer, Vaulx-en-Velin F-69120, France*
[4]*Faurecia Acoustics and Soft Trim Division, R&D Center, Route de Villemontry, Z.I. BP13, Mouzon 08210, France*
[5]*Université Paris-Est, Laboratoire Géomatériaux et Environnement, LGE EA 4508, 5 bd Descartes, Marne-la-Vallée 77454, France*

This article explores the applicability of numerical homogenization techniques for analyzing transport properties in real foam samples, mostly open-cell, to understand long-wavelength acoustics of rigid-frame air-saturated porous media on the basis of microstructural parameters. Experimental characterization of porosity and permeability of real foam samples are used to provide the scaling of a polyhedral unit-cell. The Stokes, Laplace, and diffusion-controlled reaction equations are numerically solved in such media by a finite element method in three-dimensions; an estimation of the materials' transport parameters is derived from these solution fields. The frequency-dependent visco-inertial and thermal response functions governing the long-wavelength acoustic wave propagation in rigid-frame porous materials are then determined from generic approximate but robust models and compared to standing wave tube measurements. With no adjustable constant, the predicted quantities were found to be in acceptable agreement with multi-scale experimental data and further analyzed in light of scanning electron micrograph observations and critical path considerations. © *2012 American Institute of Physics*. [doi:10.1063/1.3673523]

I. INTRODUCTION

The determination from local scale geometry of the acoustical properties, which characterize the macro-behavior of porous media, is a long-standing problem of great interest,[1–3] for instance, for the oil, automotive, and aeronautic industries. Recently, there has been a great interest in understanding the low Reynolds viscous flow, electrical, and diffusive properties of fluids in the pore structure of real porous media on the basis of microstructural parameters, as these transport phenomena control their long-wavelength frequency-dependent properties.[4–9] Each of these processes can be used to estimate the long-wavelength acoustic properties of a porous material.[10–14] Our aim in this paper is to get insight into the microstructure of real porous media and to understand how it collectively dictates their macro-scale acoustic properties from the implementation of first-principles calculations on a three-dimensional idealized periodic unit-cell.

In this purpose, one needs first to determine a unit cell which is suitable for representing the local geometry of the porous medium and, second, to solve the partial differential equations in such a cell to obtain the parameters governing the physics at the upper scale. The first problem is addressed through idealization of the real media. For instance, open-cell foams can be modeled as regular arrays of polyhedrons.

A presentation of various idealized shapes is given by Gibson and Ashby[15] for cellular solids and, more specifically, by Weaire and Hutzler[16] for foams. The second problem consists in the determination of the macroscopic and frequency-dependent transport properties, such as the dynamic viscous permeability.[4] The number of media which can be analytically addressed is deceptively small,[17] and many techniques have been developed in the literature, such as estimates combining the homogenization of periodic media and the self-consistent scheme on the basis of a bicomposite spherical pattern (see, for instance, the recent work of Boutin and Geindreau, and references therein[8,9]).

The purpose of this paper is to present a technique based on first-principles calculations of transport parameters[5] in reconstructed porous media,[18] which can be applied to model the acoustic properties of real foam samples (predominantly open-cell) and to compare its predictions to multi-scale experimental data. The main difficulty in modeling the frequency-dependent viscous and thermal parameters characterizing the dissipation through open-cell foams lies in accurately determining micro-structural characteristics and in deducing from these features how they collectively dictate the acoustical macro-behavior. Since the variability in the foam microstructures makes it very difficult to establish and apply local geometry models to study the acoustics of these foams, the use of a representative periodic cell is proposed to quantitatively grasp the complex internal structure of predominantly open-cell foam samples. Such a periodic cell, named thereafter periodic

---

a)Author to whom correspondence should be addressed. Electronic mail: camille.perrot@univ-paris-est.fr.

unit cell, has characteristic lengths, which are directly deduced from routinely available porosity and static viscous permeability measurements — two parameters practically required to determine acoustical characteristics of porous absorbents in the classical phenomenological theory.[19]

The studies on the acoustic properties derivation from the local characteristics of a porous media can be split into two classes, which address the reconstruction problem differently. The first class uses prescribed porosity and correlation length(s) for the reconstruction process or three-dimensional images of the real samples.[6] In the second class, idealization of the microstructure, whether it is granular-,[20,21] fibrous-,[22] or foam-[23-26] like types, is performed. This provides a periodic unit cell (PUC) having parameterized local geometry characteristics depending on the fabrication process, helpful for understanding the microphysical basis behind transport phenomena as well as for optimization purposes.[27]

The approach to be presented in this paper is a hybrid. From the first-principles calculations method,[5] we take the idea to compute, for three-dimensional periodic porous media models, the asymptotic parameters of the dynamic viscous $\tilde{k}(\omega)$ and thermal $\tilde{k}'(\omega)$ permeabilities[4,28] from the steady Stokes, Laplace, and diffusion-controlled reaction equations. Then, instead of using this information for comparison with direct numerical simulations of $\tilde{k}(\omega)$ and $\tilde{k}'(\omega)$ (which would require the solutions of the harmonic Stokes and heat equations to be computed for each frequency), we use these results as inputs to the analytical formulas derived by Pride *et al.*[29] and Lafarge *et al.*[30,31] As we will show, the results obtained in this manner are satisfying for the various foam samples used in the experiments.

This paper is divided into six sections. Sec. II is devoted to the direct static characterization of foam samples. Sec. III describes the methodology which is used to determine the local characteristic lengths of a three-dimensional periodic unit-cell, from which all the transport parameters are computed. Sec. IV details a hybrid numerical approach employed to produce estimates of the frequency-dependent visco-inertial and thermal responses of the foams. An assessment of the methodology through experimental results is made in Sec. V. In addition, keys for further improvements of the methodology are reported in light of scanning electron micrographs of the foam samples. Sec. VI provides a supple-

mentary justification and validation of the proposed method through conceptual and practical arguments as well as uncertainty analysis. Sec. VII concludes this paper.

II. DIRECT STATIC CHARACTERIZATION OF FOAM SAMPLES

A. Microstructure characterization

Three real and commercially available polymeric foam samples have been studied. They are denoted R_1, R_2, and R_3. These samples have been chosen for the following reason: contrary to previously studied open-cell aluminum foam samples,[23-25] their apparent characteristic pore size D is around a few tenths of a millimeter and small enough so that the visco-thermal dissipation functions characterizing their acoustical macro-behavior are, *a priori*, accurately measurable on a representative frequency range with a standard impedance tube technique.[32]

Real foam samples are disordered[33,34] and possess a complex internal structure, which is difficult to grasp quantitatively. However, our objective is to be able to quantify the local geometry of such foams by an idealized packing of polyhedral periodic unit cells (PUC). Apart from the intrinsic need for characterizing the cell morphology itself, insight into the morphology of an idealized PUC is helpful for understanding the microphysical basis behind transport phenomena.

Figure 1 shows typical micrographs of these real polyurethane foam samples (based on a polyester or polyether polyol), taken with the help of a binocular (Leica MZ6). Although X-ray microtomography analysis and scanning electron micrography (SEM) provide a precise microstructure characterization, a stereomicroscope remains affordable for any laboratory and enables reaching the primary objective related to the quantitative characterization of the foam cell shapes or, more simply stated, to verify that the local geometry model to be used will be compatible with the real disordered system under study. The maximum magnification is $\times 40$ with a visual field diameter of 5.3 mm. Foam samples were cut perpendicularly to the plane of the sheet. To get an idea of the cellular shape of these samples, the number of edges per face n was measured from 30 different locations for each material. Each location is
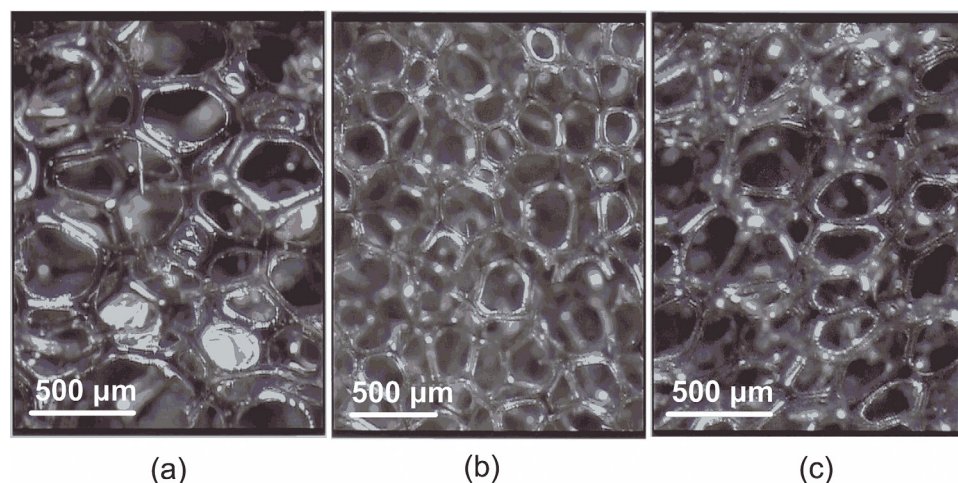

FIG. 1. (Color online) Typical micrographs of real foam samples: (a) R_1, (b) R_2, and (c) R_3. The average numbers n of edges per face for each photomicrograph are as follows: (a) R_1, $n_1 = 5.21 \pm 0.69$; (b) R_2, $n_2 = 4.94 \pm 0.56$; (c) R_3, $n_3 = 4.84 \pm 0.80$.

(a)   (b)   (c)

TABLE I. Averaged measured ligament lengths from optical photomicrographs, L_m.

Foams	Horizontal and vertical cross-sections	Horizontal cross-section	Vertical cross-sections
R_1	$L_{m1HV} = 205.0 \pm 41.6$	$L_{m1H} = 192.9 \pm 43.3$	$L_{m1V} = 211.7 \pm 39.3$
R_2	$L_{m2HV} = 229.5 \pm 57.3$	$L_{m2H} = 226.6 \pm 58.3$	$L_{m2H} = 236.5 \pm 54.5$
R_3	$L_{m3HV} = 182.4 \pm 41.7$	$L_{m3H} = 167.5 \pm 32.1$	$L_{m3H} = 193.7 \pm 44.6$

associated with one photomicrograph. For each picture, the number of analyzed faces, having continuously connected edges, is ranging between 5 and 53 with an average value of 23. From these measurements follows an average number of edges per face for each foam sample: R_1, $n_1 = 5.10 \pm 0.82$; R_2, $n_2 = 5.04 \pm 0.68$; and R_3, $n_3 = 5.03 \pm 0.71$. Next, ligaments' lengths were measured on optical micrographs of the foam samples. Since the surface contains exposed cells, whose ligament lengths are to be measured on micrographs obtained by light microscopy, great care was taken during measurements to select only ligaments lying in the plane of observation. Ligament length measurements were performed on three perpendicular cross-sections of each sample. Assuming transverse isotropy of the foam samples cellularity, results of ligament length measurements were reported in Table I and their distribution plotted in Fig. 2. Ligament thicknesses constitute also an important geometrical parameter. However, they were difficult to measure because lateral borders of the ligaments are not well defined on optical photomicrographs (due to reflections caused by thin residual membranes). Therefore, the ligament thicknesses were not primarily used.

B. Direct determination of porosity and static permeability

The porosity was non-destructively measured from the perfect gas law properties using the method described by Beranek.[35] It is found to range between 0.97 and 0.98: R_1, $\phi_1 = 0.98 \pm 0.01$; R_2, $\phi_2 = 0.97 \pm 0.01$; and R_3, $\phi_3 = 0.98 \pm 0.01$. The experimental value of the static permeability k_0 was obtained by means of accurate measurements of differential pressures across serial-mounted, calibrated, and unknown flow resistances, with a controlled steady and non-pulsating laminar volumetric air flow, as described by Stinson and Daigle[36] and further recommended in the corresponding standard ISO 9053 (method A). Results summarized in Table II are as follows: R_1, $k_0 = 2.60 \pm 0.08 \times 10^{-9}$ m^2; R_2, $k_0 = 2.98 \pm 0.14 \times 10^{-9}$ m^2; and R_3, $k_0 = 4.24 \pm 0.29 \times 10^{-9}$ m^2.

These measurements were performed at laboratory Matelys-AcV using equipments available at ENTPE (Lyon, France). To measure k_0, the volumetric airflow rates passing through the test specimens have a value of 1.6 cm^3/s. A sample holder of circular cross-sectional area was used, with a diameter of 46 mm (which allows using the same samples

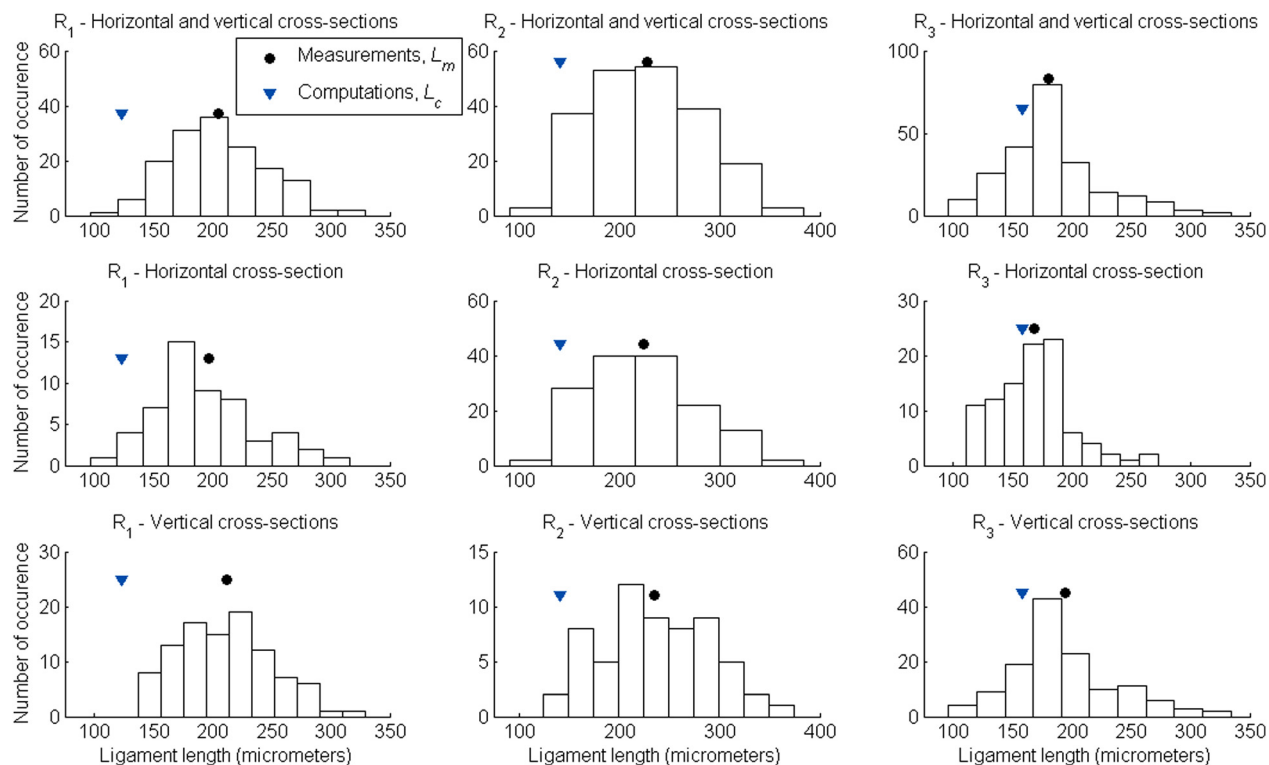FIG. 2. (Color online) Ligament length distributions for real foam samples R_1 (left), R_2 (center), and R_3 (right). Labels (●) give the measured averaged ligament lengths L_m obtained from micrographs, whereas labels (▼) indicate the computed ligament length L_c of the truncated octahedron unit-cell used for numerical simulations.

TABLE II. Comparison between computed and measured macroscopic parameters.

Foams	Method	$\phi(-)$	$\Lambda'(\mu m)$	$k_0(m^2)$	$\alpha_0(-)$	$\Lambda(\mu m)$	$\alpha_\infty(-)$	$k_0'(m^2)$	α_0'
R_1	Computations		506		1.22	297	1.02	5.01×10^{-9}	1.13
	Measurements[a,b]	0.98		2.60×10^{-9}					
	Characterization[c,d]		440			129	1.12	8.30×10^{-9}	
R_2	Computations		477		1.26	279	1.02	5.85×10^{-9}	1.14
	Measurements[a,b]	0.97		2.98×10^{-9}					
	Characterization[c,d]		330			118	1.13	9.70×10^{-9}	
R_3	Computations		647		1.22	373	1.01	8.18×10^{-9}	1.13
	Measurements[a,d]	0.98		4.24×10^{-9}					
	Characterization[c,d]		594			226	1.06	13.10×10^{-9}	

[a]Reference 35.
[b]Reference 36.
[c]Reference 54.
[d]Reference 55.

for impedance tube measurements). This corresponds to a source, such as there is essentially laminar unidirectional airflow entering and leaving the test specimen at values just below 1 mm/s and for which quasi-static viscous permeability measurements are supposed to be independent of volumetric airflow velocity.

III. PREDICTION OF TRANSPORT PROPERTIES FROM A THREE-DIMENSIONAL PERIODIC UNIT-CELL

A. The local geometry

As observed from the micrographs, the network of ligaments appears to be similar to a lattice, within which the ligaments delimit a set of polyhedra. In this work, it is therefore considered that a representation of the microstructure, which can be deduced from this observation, is a packing of identical polyhedra.

More precisely, truncated octahedra with ligaments of circular cross section shapes and a spherical node at their intersections were considered, as in a similar work on thermal properties of foams.[37] It will be shown that the FEM results are not significantly affected by this approximation (see Secs. III and VI), even if the real cross-section of ligaments can be rather different.[38] Note that appropriate procedures were derived to account for sharp-edged porous media.[39,40]

A regular truncated octahedron is a 14-sided polyhedron (tetrakaidecahedron), having six squared faces and eight hexagonal faces, with ligament lengths L and thicknesses $2r$. The average number of edges per face, another polyhedron shape indicator, is equal to $(6 \times 4 + 8 \times 6)/14 \approx 5.14$ and close to the experimental data presented in Sec. II A. The cells have a characteristic size D equal to $(2\sqrt{2})L$ between two parallel squared faces. An example of regular truncated octahedron for such packings is given in Fig. 3.

The simplest macroscopic parameter characterizing a porous solid is its open porosity, defined as the fraction of the interconnected pore fluid volume to the total bulk volume of the porous aggregate, ϕ. The porosity of such a packed polyhedron sample might be expressed as a function of the aspect ratio $L/2r$,

$$\phi = 1 - \left(\frac{3\sqrt{2}\pi}{16}\right)\left(\frac{2r}{L}\right)^2 - \left(\frac{\sqrt{2}\pi C_1}{16}\right)\left(\frac{2r}{L}\right)^3, \quad (1)$$

with $C_1 = -f^3 + 2(f^2 - 1)\sqrt{f^2 - 1}$, and f is a node size parameter related to the spherical radius R by $R = f \times r$, with $f \geq \sqrt{2}$. This last constraint on the node parameter ensures that the node volume is larger than the volume of the connecting ligaments at the node.

The second parameter, which is widely used to characterize the macroscopic geometry of porous media and, thus, polyhedron packing, is the specific surface area S_p, defined as the total solid surface area per unit volume. The hydraulic radius is defined as twice the ratio of the total pore volume to its surface area. This characteristic length may also be referred to as the "thermal characteristic length" Λ' in the context of sound absorbing materials,[41] so that $\Lambda' = 2\phi/S_p$. As for the porosity, the "thermal characteristic length" can be expressed in terms of the microstructural parameters by

$$\Lambda' = \left[\frac{16\sqrt{2}\left/\left(\frac{2r}{L}\right)^3 - 6\pi\left/\left(\frac{2r}{L}\right) - 2\pi C_1\right.\right.}{3\pi\left(2\left/\frac{2r}{L} + C_2\right.\right)}\right] \times r, \quad (2)$$

with $C_2 = -f^2 + 2(f - 1)\sqrt{f^2 - 1}$.

It might be useful to specify that, by definition, Eqs. (1) and (2) are valid in principle only for foams with non-elongated and fully reticulated cells.
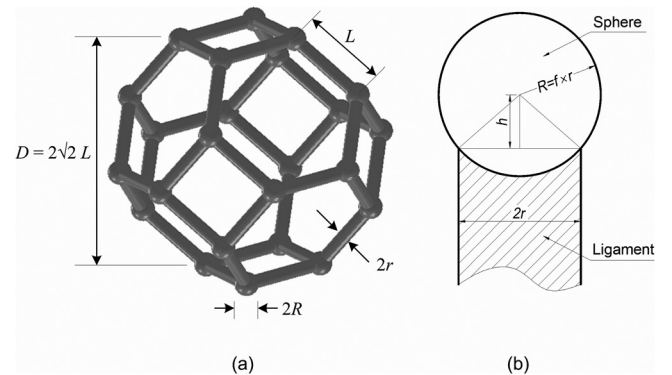

FIG. 3. Basic 3D periodic foam model geometry: (a) a regular truncated octahedron with ligaments of circular cross-section shape (length L, radius r) and (b) spherical nodes (radius R) at their intersections. Note that f is a spherical node size parameter, which is set to 1.5.

B. Determination of the unit cell aspect ratio from porosity

When a laboratory measurement of porosity is available, the unit-cell aspect ratio $L/2r$ can be identified through Eq. (1). For a given value of the spherical node size parameter f, the unit-cell aspect ratio $L/2r$ is given by the solution of a cubic equation that has only one acceptable solution.

Once $2r/L$ is obtained, Eq. (2) gives r if a laboratory measurement of S_p is available. Then, the idealized geometry of the foam could be considered as completely defined. The main problem in this method is that the specific surface area evaluation from non-acoustical measurements, such as the standard Brunauer, Emmett, and Teller method (BET)[42,43] based on surface chemistry principles, is not routinely available. Moreover, the application of physical adsorption is usually recommended for determining the surface area of porous solids classified as microporous (pore size up to 2 nm) and mesoporous (pore size 2 to 50 nm). This tends to promote alternative techniques for macropore size analysis (i.e., above 50 nm width).[44] In fact, the most widely measured parameter after the porosity to characterize the physical macro-behavior of real porous media is unarguably the static viscous (or hydraulic) intrinsic permeability k_0, as defined in Sec. III C 1, a quantity having units of a surface (squared length).

Therefore, obtaining the local characteristic sizes of the PUC will be performed thereafter in four steps. Step 1 consists of acquiring the aspect ratio $L/2r$ from the porosity measurements, as explained before. For a given spherical node size parameter, this produces all characteristic length ratios of the cell. At this stage, the ligament length of the cell is still unknown, but a non-dimensional PUC can be built. Step 2 is to characterize the permeability of the foam from routine measurements. Step 3 is to get the permeability of the set of non-dimensional periodic cells from first principle calculations. As explained before, the non-dimensional cell has a unit side of square faces. The finite element computation described thereafter implemented on the non-dimensional cell produces the non-dimensional permeability k_d. Let D_h be the side of square faces of homothetic periodic cells producing the static permeability k_0. Then, a simple computation shows that $k_0 = D_h^2 \times k_d$. Finally, comparing the non-dimensional permeability to the true permeability produces, in step 4, the size of the PUC. All other parameters are obtained from the non-dimensional results through a similar scaling.

C. First principles calculations of transport properties

Previous studies[30,31] have shown how the long-wavelengths acoustic properties of rigid-frame porous media can be numerically determined by solving the local equations governing the asymptotic frequency-dependent visco-thermal dissipation phenomena in a periodic unit cell with the adequate boundary conditions. In the following, it is assumed that $\lambda \gg D$, where λ is the wavelength of an incident acoustic plane wave. This means that, for characteristic lengths on the order of $D \sim 0.5$ mm, this assumption is valid for frequencies reaching up to a few tens of kHz. The asymp-totic macroscopic properties of sound absorbing materials are computed from the numerical solutions of:

(1) the low Reynolds number viscous flow equations (the static viscous permeability k_0 and the static viscous tortuosity α_0);
(2) the non-viscous flow or inertial equations (the high-frequency tortuosity α_∞ and Johnson's velocity weighted length's parameter Λ);
(3) the equations for thermal conduction (the static thermal permeability k_0' and the static thermal tortuosity α_0').

1. Viscous flow

At low frequencies or in a static regime, when $\omega \to 0$, viscous effects dominate and the slow fluid motion in steady state regime created in the fluid phase Ω_f of a periodic porous medium having a unit cell Ω is solution of the following boundary value problem defined on Ω by:[45]

$$\eta \Delta \mathbf{v} - \nabla \mathsf{p} = -\mathsf{G}, \quad \text{in } \Omega_f, \qquad (3)$$

$$\nabla . \mathbf{v} = 0, \quad \text{in } \Omega_f, \qquad (4)$$

$$\mathbf{v} = 0, \quad \text{on } \partial\Omega, \qquad (5)$$

$$\mathbf{v} \text{ and } \mathsf{p} \text{ are } \Omega - \text{periodic}, \qquad (6)$$

where $\mathsf{G} = \nabla \mathsf{p}^m$ is a macroscopic pressure gradient acting as a source term, η is the viscosity of the fluid, and $\partial\Omega$ is the fluid-solid interface. This is a steady Stokes problem for periodic structures, where $\mathbf{v}$ is the Ω-periodic velocity, p is the Ω-periodic part of the pressure fields in the pore verifying $\langle \mathsf{p} \rangle = 0$, and the symbol $\langle \rangle$ indicates a fluid-phase average. It can be shown that the components v_i of the local velocity field are given by

$$v_i = -\frac{k_{0ij}^*}{\eta} G_j. \qquad (7)$$

The components of the static viscous permeability tensor are then specified by[8,9]

$$k_{0ij} = \phi \left\langle k_{0ij}^* \right\rangle \qquad (8)$$

and the components of the tortuosity tensor are obtained from

$$\alpha_{0ij} = \left\langle k_{0pi}^* k_{0pj}^* \right\rangle \Big/ \left\langle k_{0ii}^* \right\rangle \left\langle k_{0jj}^* \right\rangle, \qquad (9)$$

wherein the Einstein summation notation on p is implicit. In the present work, the symmetry properties of the microstructure under consideration imply that the second order tensors $\mathbf{k}_0$ and $\boldsymbol{\alpha}_0$ are isotropic. Thus, $k_{0ij} = k_0 \delta_{ij}$ and $\alpha_{0ij} = \alpha_0 \delta_{ij}$, where δ_{ij} is the Kronecker symbol.

2. Inertial flow

At the opposite frequency range, when ω is large enough, the viscous boundary layer becomes negligible and the fluid tends to behave as a perfect one, having no viscosity except in a boundary layer. In these conditions, the perfect incompressible fluid formally behaves according to the problem of electric conduction,[46–48] i.e.,

$$\mathbf{E} = -\nabla\varphi + \mathbf{e}, \quad \text{in } \Omega_\text{f}, \tag{10}$$

$$\nabla \cdot \mathbf{E} = 0, \quad \text{in } \Omega_\text{f}, \tag{11}$$

$$\mathbf{E} \cdot \mathbf{n} = 0, \quad \text{on } \partial\Omega, \tag{12}$$

$$\varphi \text{ is } \Omega - \text{periodic}, \tag{13}$$

where $\mathbf{e}$ is a given macroscopic electric field, $\mathbf{E}$ the solution of the boundary problem having $-\nabla\varphi$ as a fluctuating part, and $\mathbf{n}$ is unit normal to the boundary of the pore region.

Then, the components $\alpha_{\infty ij}$ of the high frequency tortuosity tensor can be obtained from[31]

$$e_i = \alpha_{\infty ij}\langle E_j \rangle. \tag{14}$$

In the case of isotropy, the components of the tensor $\boldsymbol{\alpha}_\infty$ reduce to the diagonal form $\alpha_{\infty ij} = \alpha_\infty \delta_{ij}$. In this case, the tortuosity can also be obtained from the computation of the mean square value of the local velocity through

$$\alpha_\infty = \frac{\langle \mathbf{E}^2 \rangle}{\langle \mathbf{E} \rangle^2}. \tag{15}$$

As for the low frequency tortuosity, an extended formula can be used for anisotropic porous media. Having solved the cell conduction problem, the viscous characteristic length Λ can also be determined (for an isotropic medium) by[4]

$$\Lambda = 2 \frac{\displaystyle\int_\Omega \mathbf{E}^2 dV}{\displaystyle\int_{\partial\Omega} \mathbf{E}^2 dS}. \tag{16}$$

3. Thermal effect

When the vibration occurs, the pressure fluctuation induces a temperature fluctuation inside the fluid, due to the constitutive equation of a thermally conducting fluid. If one considers the solid frame as a thermostat, it can be shown that the mean excess temperature in the air $\langle \tau \rangle$ is proportional to the mean time derivative of the pressure $\partial\langle p \rangle/\partial t$. This thermal effect is described by $\langle \tau \rangle = (k'_0/\kappa)\partial\langle p \rangle/\partial t$, where $\langle \tau \rangle$ is the macroscopic excess temperature in air, κ is the coefficient of thermal conduction, and k'_0 is a constant. The constant k'_0 is often referred to as the "static thermal permeability". As the usual permeability, it has the dimensions of a surface and was thus named by Lafarge *et al.*[28] It is related to the "trapping constant" Γ of the frame by $k'_0 = 1/\Gamma$.[47] In the context of diffusion-controlled reactions, it was demonstrated by Rubinstein and Torquato[49] that the trapping constant is related to the mean value of a "scaled concentration field" $u(\mathbf{r})$ by

$$\Gamma = 1/\langle u \rangle, \tag{17}$$

where $u(\mathbf{r})$ solves

$$\Delta u = -1, \quad \text{in } \Omega_\text{f}, \tag{18}$$

$$u = 0, \quad \text{on } \partial\Omega. \tag{19}$$

It is worthwhile noticing that Δu is dimensionless. Therefore, u and k'_0 have the dimension of a surface.

Similarly to tortuosity factors obtained from viscous and inertial boundary value problems, a "static thermal tortuosity" is given by

$$\alpha'_0 = \frac{\langle u^2 \rangle}{\langle u \rangle^2}. \tag{20}$$

D. Dimensioning the unit cell from static permeability

The permeability k_0 obtained from a computational implementation of the low Reynolds number viscous flow equations, as described in Sec. III C 1, can be determined from the non-dimensional PUC. Then, it is well known that, for all homothetic porous structures, the permeability k_0 is proportional to the square of the hydraulic radius, which was previously renamed as "thermal characteristic length" Λ'. Thus, for an isotropic medium, a generic linear equation $k_0 = S \times \Lambda'^2 + 0$ must exist, where S is the non-dimensional slope to be numerically determined. At a fixed porosity, S depends only on the morphology of the unit cell and not on the size of the cell.

As a consequence, knowing k_0 from experimental measurements and S from computations on the non-dimensional structure produces the specific thermal length Λ', and $D_h = \Lambda'\sqrt{S/k_d}$. Making use of Eqs. (1) and (2), local characteristic lengths L and r follow. Hence, there are *a priori* two routinely available independent measurements to be carried out in order to define the foam geometry: the porosity ϕ and the static viscous permeability k_0. This method for periodic unit-cell reconstruction circumvents the necessary measure of the specific surface area. As previously mentioned, all this procedure assumes that the spherical node size parameter f is known. In our computations, f was set to 1.5. This value respects the constraint $f \geq \sqrt{2}$ and is in a rather good agreement with microstructural observations, considering the absence of lump at the intersection between ligaments (see Fig. 1). Application of the above procedure yields the local characteristic sizes of a unit cell ligament for each foam sample: R_1, $L_1 = 123 \pm 13\ \mu m$ ($L_{m1} = 205 \pm 42\ \mu m$), $2r_1 = 19 \pm 7\ \mu m$ ($2r_{m1} = 31 \pm 7\ \mu m$); R_2, $L_2 = 141 \pm 12\ \mu m$ ($L_{m2} = 229 \pm 57\ \mu m$), $2r_2 = 27 \pm 7\ \mu m$ ($2r_{m2} = 36 \pm 8\ \mu m$); and R_3, $L_3 = 157 \pm 19\ \mu m$ ($L_{m2} = 182 \pm 42\ \mu m$), $2r_3 = 25 \pm 10\ \mu m$ ($2r_{m3} = 30 \pm 6\ \mu m$). Comparison between computed and measured characteristic sizes estimations are thoroughly discussed in Secs. V and VI (see also Appendix C).

Uncertainties for the critical characteristic sizes of the PUC correspond to the standard deviations computed when considering input macroscopic parameters ϕ and k_0 associated with their experimental uncertainties. This enables evaluating the impact of porosity and permeability measurement uncertainties on the estimation of local characteristic lengths.

Note that, for anisotropic medium, k_0 varies with the direction of the airflow inside the foam (see, for example, the flow resistivity tensors presented in Ref. 50) and the equation $k_0 = S \times \Lambda'^2$ is no more valid. Thus, the size of the PUC depends on the direction of the airflow used during the static permeability measurements. To be more complete, k_0 should be measured along three directions, leading to three pairs of
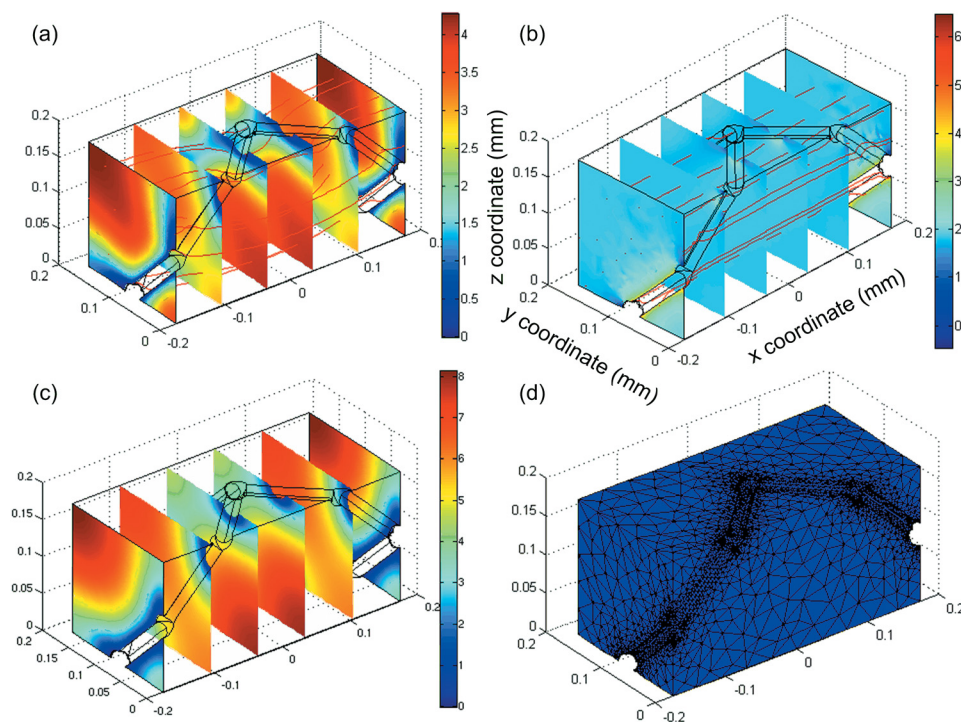
FIG. 4. (Color online) Asymptotic fields for 1/4th of the reconstructed foam sample period R_1: (a) low-frequency scaled velocity field k_{0xx}^* [$\times 10^{-9}$ m^2], (b) high-frequency scaled velocity field $E_x/\nabla\varphi$ [–] for an external unit field e_x, (c) low-frequency scaled temperature field k_0' [$\times 10^{-9}$ m^2], and (d) corresponding mesh domain with 41 372 lagrangian P_2P_1 tetrahedral elements.

critical lengths to estimate the possible anisotropy. This issue will be addressed in a forthcoming paper.

E. Results on asymptotic transport properties obtained from finite element modeling

An example of calculated viscous flow velocity, inertial flow velocity, and scaled concentration fields obtained through a finite element mesh is shown in Fig. 4 for foam sample R_1. The number of elements and their distribution in the fluid phase regions of the PUC were varied, with attention paid especially to the throat and the near-wall areas, to examine the accuracy and convergence of the field solutions. The symmetry properties of the permeability/tortuosity tensors were also checked[51] as a supplementary test on convergence achievement. As previously noticed by several authors, such as Martys and Garboczi,[52] due to the slip condition, the fluid flow paths are more homogeneous for the electric-current paths than for the viscous fluid flow.

Direct numerical computations of the complete set of macroscopic parameters were performed in reconstructed unit cells from adequate asymptotic field averaging, as described in Secs. III C 1–3. Results are reported in Table II. Some values are compared to estimations obtained from impedance tube measurements (see Sec. V A).

We also note that our results are consistent with the inequalities $\alpha_0 > \alpha_\infty$ and $\alpha_0/\alpha_\infty \geq \alpha_0' > 1$, as introduced by Lafarge[31] from physical reasons.

IV. ESTIMATES OF THE FREQUENCY-DEPENDENT VISCO-INERTIAL AND THERMAL RESPONSES BY A HYBRID NUMERICAL APPROACH

The acoustic response of foams depends on dynamic viscous permeability and "dynamic thermal permeability". Both of these parameters could be obtained from dynamic FEM computations, as in Ref. 20. The approach presented here relies on the fact that the finite element computations presented previously are easy to implement and provide the asymptotic behavior for both dynamic "permeabilities". This asymptotic behavior constitutes the input data for the models, which are used for predicting the full frequency range of the dynamic "permeabilities". Therefore, the hybrid approach employed in our study makes use of the asymptotic parameters of the porous medium obtained by finite elements. Then, it will be possible to provide the dynamic permeabilities and to compare these values to experimental ones. In a first step, the three different models, which are used to build the dynamic permeabilities from asymptotic parameters, are briefly recalled.

Johnson *et al.*[4] and, later, Pride *et al.*[29] considered the problem of the response of a simple fluid moving through a rigid porous medium and subjected to a time harmonic pressure variation across the sample. In such systems, they constructed simple models of the relevant response functions, the effective dynamic viscous permeability $\tilde{k}(\omega)$, or effective dynamic tortuosity $\tilde{\alpha}(\omega)$. The main ingredient to build these models is to account for the causality principle and, therefore, for the Kramers-Kronig relations between real and imaginary parts of the frequency-dependent permeability. The parameters in these models are those which correctly match the frequency dependence of the first one or two leading terms on the exact results for the high- and low-frequency viscous and inertial behaviors.

Champoux and Allard[3,41] and, thereafter, Lafarge *et al.*,[28,30,31] in adopting these ideas to thermally conducting fluids in porous media, derived similar relations for the frequency dependence of the so-called effective "dynamic thermal permeability" $\tilde{k}'(\omega)$ or effective dynamic compressibility $\tilde{\beta}(\omega)$, which varies from the isothermal to the adiabatic value when frequency increases. The model for effective dynamic permeabilities were shown to agree with those calculated

directly or independently measured. An important feature of this theory is that all of the parameters in the models can be calculated independently, most of them being in addition directly measurable in non-acoustical experimental situations. In this regard, these models are very attractive, because they avoid computing the solution of the full frequency range values of the effective permeabilities/susceptibilities. These models are recalled in Appendix B. They are based on simple analytic expressions in terms of well-defined high- and low-frequency transport parameters, which can be determined from first principles calculations (Secs. III C 1–3).

Such a hybrid approach was used by Perrot, Chevillotte, and Panneton in order to examine micro-/macro relations linking local geometry parameters to sound absorption properties for a two-dimensional hexagonal structure of solid fibers (Ref. 25). Here, this method is completed by the use of easily obtained parameter (porosity ϕ and static viscous permeability k_0) of real foam samples, as explained previously and by utilizing three-dimensional numerical computations.

As explicated, the comparison between non-dimensional permeability obtained from finite element results and the measured permeability provides the thermal characteristic length Λ', and five remaining input parameters for the models, α_0, α_∞, Λ, k_0', and α_0' can be obtained by means of first-principles calculations by appropriate field-averaging in the PUC.

Finally, we considered the predictions of the three models for the effective dynamic permeabilities, described in Appendix B. In summary, the Johnson-Champoux-Allard (JCA) model, which uses the 5 parameters (ϕ, k_0, α_∞, Λ, Λ'), Johnson-Champoux-Allard-Lafarge model (JCAL), which uses, in addition, k_0', and Johnson-Champoux-Allard-Pride-Lafarge (JCAPL) model, which uses the full set of parameters (ϕ, k_0, k_0', α_∞, Λ, Λ', α_0, and α_0').

V. ASSESSMENT OF THE METHODOLOGY THROUGH EXPERIMENTAL RESULTS

A. Experimental results and comparison with numerical results

Experimental values of the frequency-dependent visco-inertial and thermal responses were provided using the impedance tube technique by Utsuno *et al.*,[32] in which the equivalent complex and frequency-dependent characteristic impedance $\tilde{Z}_{eq}(\omega)$ and wave number $\tilde{q}_{eq}(\omega)$ of each material were measured and the equivalent dynamic viscous permeability $\tilde{k}_{eq}(\omega) = \tilde{k}(\omega)/\phi$, the equivalent dynamic thermal permeability $k_{eq}'(\omega) = k'(\omega)/\phi$, and the sound absorption coefficient at normal incidence $A_n(\omega)$, derived from $\tilde{Z}_{eq}(\omega)$ and $\tilde{q}_{eq}(\omega)$.

One main objective of this section is to produce a comparison between hydraulic and thermal permeabilities coming from experimental results and from numerical computations. In this context, intermediate results were obtained for the acoustic parameters of the JCAL model through the characterization method described in Ref. 54 for viscous dissipation and Ref. 55 for thermal dissipation. This kind of characterization also provides the viscous (respectively thermal) transition frequencies between viscous and inertial regimes (respectively isothermal and adiabatic), $f_v = \nu\phi/2\pi k_0\alpha_\infty$ ($f_t = \nu'\phi/2\pi k_0'$). These results will be

thereafter referenced to in the figures and tables as obtained from "characterization".

Figures 5, 6, and 7 produce the sound absorption coefficient simultaneously with the estimation of hydraulic and
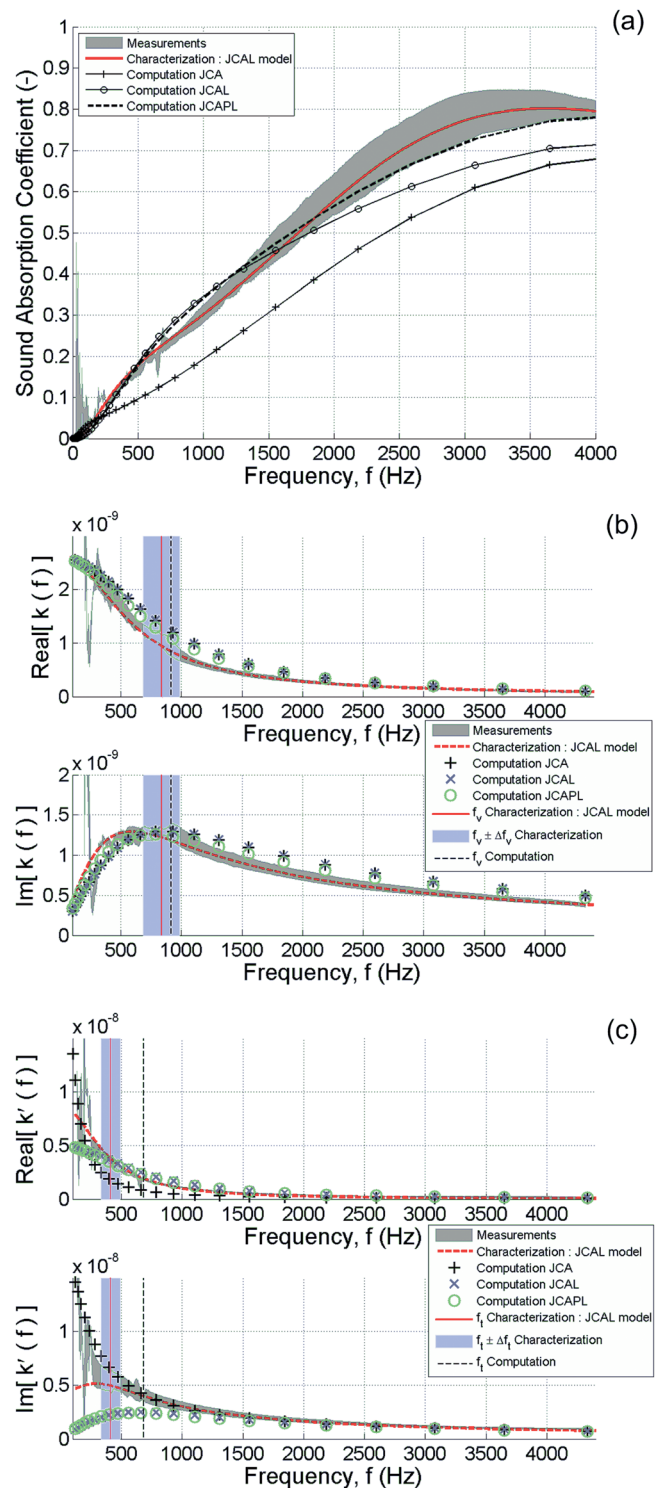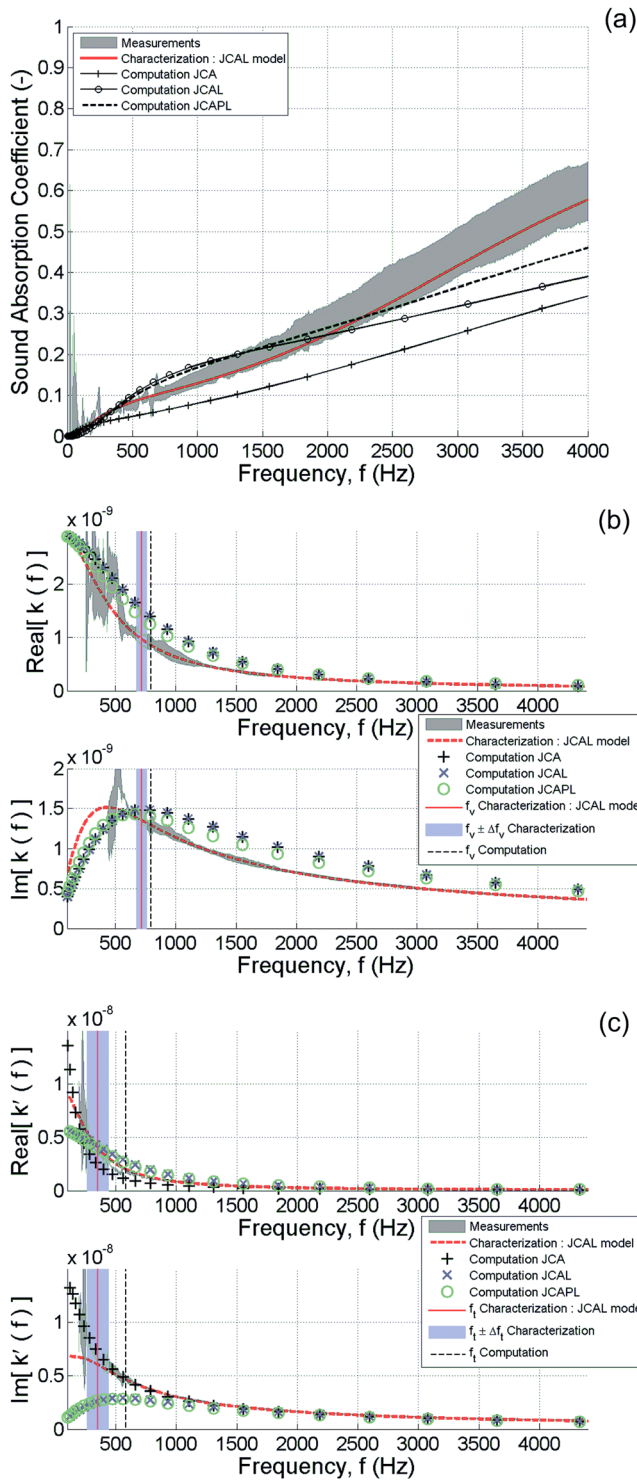

FIG. 5. (Color online) (a) Normal incidence sound absorption coefficient, (b) dynamic viscous permeability $k(f)$, and (c) dynamic thermal permeability $k'(f)$ for foam sample R_1: comparison between measurements (Ref. 32), characterization (Refs. 54 and 55 combined with JCAL model described in Appendix B), and computations (this work). The errors of the characterizations of the transition frequencies Δf_v and Δf_t follow from the errors of the measurements of ρ_0, ϕ, k_0, and from the errors of the characterizations of α_∞ and k_0' through Gauss' law of error propagation. Sample thickness: 25 mm.
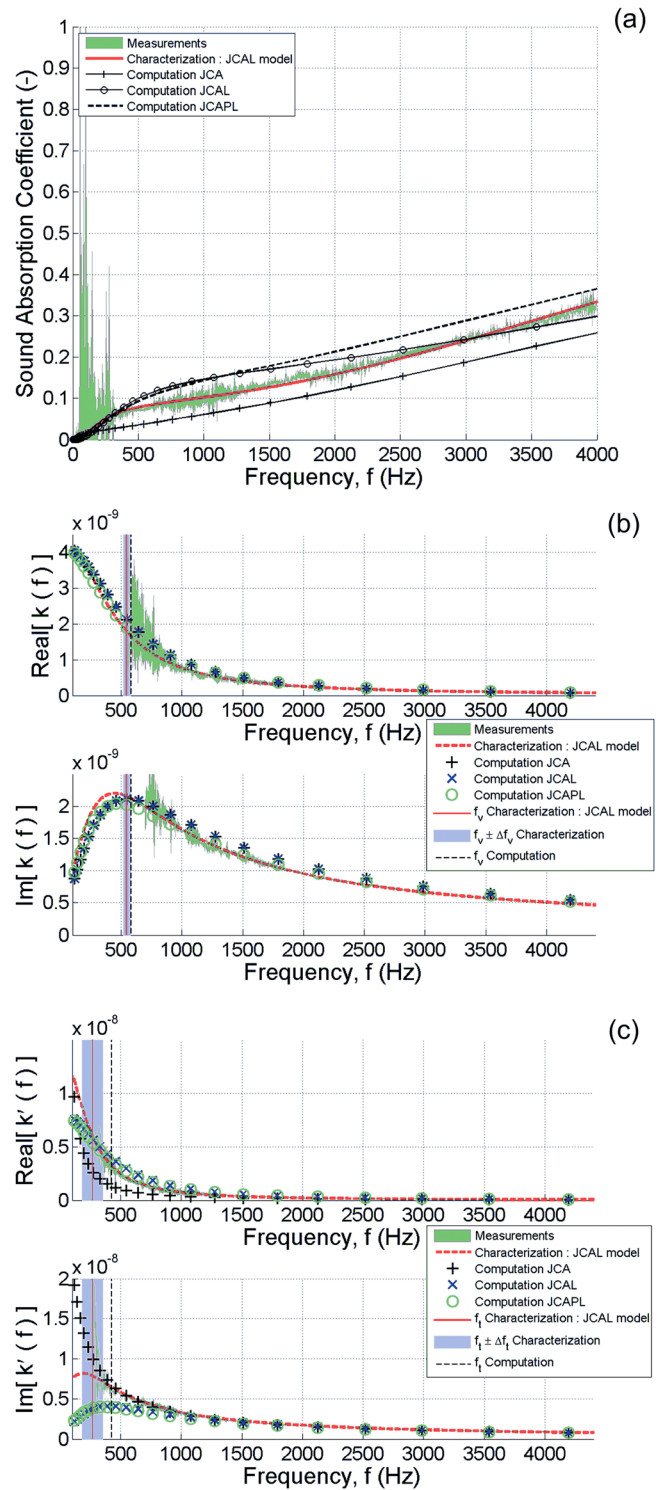
FIG. 6. (Color online) (a) Normal incidence sound absorption coefficient, (b) dynamic viscous permeability $k(f)$, and (c) dynamic thermal permeability $k'(f)$ for foam sample R$_2$: comparison between measurements (Ref. 32), characterization (Refs. 54 and 55 combined with JCAL model described in Appendix B), and computations (this work). The errors of the characterizations of the transition frequencies Δf_v and Δf_t follow from the errors of the measurements of ρ_0, ϕ, k_0, and from the errors of the characterizations of α_∞ and k_0' through Gauss' law of error propagation. Sample thickness: 15 mm.

FIG. 7. (Color online) (a) Normal incidence sound absorption coefficient, (b) dynamic viscous permeability $k(f)$, and (c) dynamic thermal permeability $k'(f)$ for foam sample R$_3$: comparison between measurements (Ref. 32), characterization (Refs. 54 and 55 combined with JCAL model described in Appendix B), and computations (this work). The errors of the characterizations of the transition frequencies Δf_v and Δf_t follow from the errors of the measurements of ρ_0, ϕ, k_0, and from the errors of the characterizations of α_∞ and k_0' through Gauss' law of error propagation. Sample thickness: 15 mm.

thermal permeability obtained from experiment, from characterization, and from numerical computations. Because all viscous and thermal shape factors recalled in Appendix B significantly diverge from unity, large deviations are noticea-

ble between JCA, JCAL, and JCAPL semi-phenomenological models. This tends to promote JCAL and JCAPL as the models to be numerically used for the real polymeric foam samples under study. Characterized values for M' thermal shape

factors are on the order of 0.35, 0.73, and 0.30, respectively, for foam samples R_1, R_2, and R_3. Computed values are of similar magnitude: 0.16, 0.21, and 0.16. For real foam samples R_1 and R_3, the ratio between characterized and computed thermal shape factors is around 2, whereas, for foam sample R_2, it reaches approximately 3. Because we largely overestimated the thermal length for foam sample R_2 (that exhibits anisotropy, see the end of Sec. V A and Sec. V B), the later overestimate is amplified through the square involved in M' computation (Appendix B). We note that significant deviations from unity of the thermal shape factors characterized for real porous materials were already observed in the literature, for instance, for the glass wool ($M' = 1.34$) and rock wool ($M' = 2.84$) samples studied in Ref. 55 and Table II. The large deviations from unity for the thermal shape factors reveal the striking importance of the k'_0 parameter in the accurate description of the frequency-dependent thermal dissipation effects (see also Figs. 9 and 10 of the previously mentioned reference). Once again, at some computed shape factors P and P' well below unity (0.29–0.4), the effect of α_0 and α'_0 is strong and has a large frequency range. One might, therefore, expect a frequency-dependent acoustical macro-behavior with the JCAPL model for the three real foam samples under study very distinct from the one described by the JCAL model. Instead, the computed values of $\tilde{k}(\omega)$ and $A_n(\omega)$ are of different magnitudes, especially around and after the viscous transition frequencies (since the low frequency behavior of $\tilde{k}(\omega)$ is essentially governed by k_0). Despite the simplicity of the local geometry model used to study the multi-scale acoustic properties of real foam samples predominantly open-cell, there is a relatively good agreement between computed (present microstructural method), measured (impedance tube measurements), and characterized dynamic quantities: $\tilde{k}_{eq}(\omega)$, $\tilde{k}'_{eq}(\omega)$, and $A_n(\omega)$. Furthermore, the general trend given in terms of normal incidence sound absorption coefficient by our microstructural approach appears as being particularly relevant if we notice that it requires only ϕ and k_0 as input parameters and proceeds without any adjustable parameter.

Discrepancies between measured and computed sound absorption coefficients at normal incidence can be primarily explained from the comparison of a set of parameters obtained from numerical results and from the characterization method reported in Table II, namely Λ', Λ, α_∞, and k'_0. Note, however, that this comparison is limited by the fact that the characterization method is JCAL model-dependent. From that comparison, it can be seen that:

- α_∞ is slightly underestimated by the numerical results;
- Λ' is slightly overestimated by the numerical results for R_1 and R_3, but overestimated by around 44% for R_2;
- Λ is overestimated by a factor between 1.6 and 2.4;
- k_0' is underestimated (around 40% for all results).

Considering primarily visco-inertial dissipation phenomena, the most significant difference is the large overestimation provided for Λ. This means that, at high frequencies, the window size of the local geometry model, which respectively plays the role of weighting the velocity field for Λ and rapid section changing for α_∞ by their small openings (the squares in the case of a truncated octahedron unit-cell) is

presumably overestimated by a monodisperse, isotropic, and membrane-free local geometry model. Consequently, an improvement of the local geometry model would result in the introduction of a second set of characteristic sizes.

A local geometry model having ligaments with concave triangular cross-section shapes and a fillet at the cusps was also implemented (not detailed here). For circular cross-section shapes, the deviations between computed and characterized thermal lengths are on the order of 15%, 44%, and 9% for foam samples R_1, R_2, and R_3, respectively (Table II). It is also worth to mention that taking into account the inner concave triangular nature of the ligament cross-section shapes reduces discrepancies between computed and characterized thermal lengths, since the relative differences were found to decrease to 3%, 25%, and 8%, respectively. The erroneous underestimation of the $2r/L$ ratio introduced by the circular cross-section shape model does not exceed 10%.

Λ' large overestimation for R_2 might be due to the cell elongation of the real foam sample (see Sec. V B for cell elongation evidences). Indeed, from a purely geometrical point of view, it can be shown by using an elongated tetrakaidecahedron unit cell model[56] that a cell elongation of the tetrakaidecahedron may be obtained without modification of the ligaments lengths and thicknesses if there is an increase of the inclination angle θ (which defines the orientation of the hexagonal faces with respect to the rise direction as well as the obtuse angle of the vertical diamond faces, 2θ). By doing so, one can analytically derive a monotonic decreasing thermal length Λ' with increasing degree of anisotropy (DA). For instance, $\Lambda' = 350\,\mu m$ with DA = 1.79.

It is further fruitful for our purpose to think about the implications of a thermal reticulation process on the cellular morphology of real foam samples. During the thermal reticulation process, a high temperature, high speed flame front removes most of the cell membranes from the foam. This process, which occurs as the membranes have a high surface area to mass ratio, melts the cell membranes and fuses them around the main cell ligaments. Consequently, membranes associated to large windows are predominantly depolymerized, and membranes attached to the smallest windows tend to be maintained. As a result, even apparently membrane-free foam samples conserve very small apertures around the smallest windows. This could explain why the open cell PUC generates an overestimation of the viscous length (by around 65%) for foam sample R_3.

The purpose of the following is to examine more thoroughly the microstructure in order to provide some means aimed at improving the methodology.

B. Keys for further improvements of the methodology

A supplementary visual cell inspection is given by electron micrographs at very low magnification, as presented in Fig. 8. These pictures were obtained with an environmental scanning electron microscope (ESEM), S-3000 N HITACHI, using an accelerating voltage of 5 or 15 kV, available at Université de Sherbrooke. The characteristic ligament length L_c obtained for the periodic cell is reported on the micrographs, which allows a first visual comparison between observed and computed cell sizes.
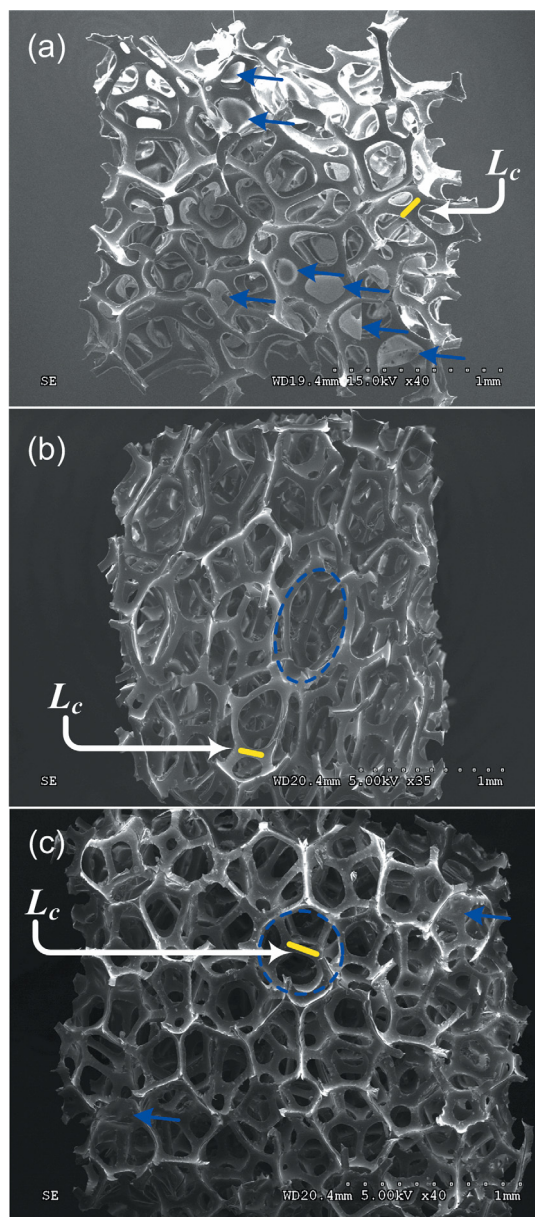
FIG. 8. (Color online) Typical scanning electron microscope images of real foam samples. (a) R_1, showing a relatively great number of membranes (indicated by arrows) compared to R_2 and R_3 foams. (b) R_2, having a degree of anisotropy equal to 1.75, as illustrated with a superimposed ellipse. (c) R_3, exhibits only few isolated residual membranes (thermal reticulation process), with rather spherical pore shapes (schematically represented by a circle). For each real foam sample, a line corresponding to the specific length L_c clearly shows the typical size of an opening which could participate to a critical path.

Another element of discussion is provided in Fig. 2, where the distribution of the measured ligament lengths is reported (together with its mean value L_m), simultaneously with the length L_c obtained from the numerical results and from the calibration coming from (k_0, ϕ).

The characteristic ligament length L_c of the local geometry model provides a basis for understanding the influence of certain local geometry features, such as membrane effects and cell anisotropy, on the static viscous permeability of the real foam samples — in connection with ligaments length distribution.

More precisely, if the distribution of the ligament lengths is sharply peaked, one would expect the overall system behavior to be similar to that of the individual elements. This is a configuration close to the one observed for foam sample R_3, where only isolated residual membranes (thermal reticulation process) and no specific cell elongation were observed, as illustrated on the electron micrograph in Fig. 8(c), and for which the distribution of the ligaments length combining horizontal and vertical surfaces is relatively sharp (see Fig. 2, top right). As a result, the ligaments' length of the local geometry model for foam sample R_3 is (actually lower and) relatively close to the averaged value measured on the micrographs, especially for the horizontal surface, through which permeability measurements were performed ($L_c = 158\,\mu$m, $L_{m3H} = 167\,\mu$m, and $L_{m3H}/L_c = 1.06$).

On the other hand, if the distribution is broader, as shown for foam sample R_2 in Fig. 2 (top center), because of cell elongation, as it can be seen in Fig. 8(b), the critical path — made by the small windows at the openings of the cells — is expected to dominate (in Fig. 2, for the horizontal surface $L_{m2H} = 227\,\mu$m, whereas $L_c = 141\,\mu$m and L_{m2H}/L_c is now equal to 1.61).

Similarly, as observed for foam sample R_1 in Fig. 8(a), the presence of membranes occludes or significantly reduces the size of some windows, which might belong to unit-cells in the class of local permeability sites k_{ij} (in the sense of critical path considerations, see Appendix A) much greater or of the order of k_c. This has, in addition, the effect of disconnecting some critical subnetworks. In this later case, the unit-cells, which were belonging to the permeability sites with $k_{ij} \le k_c$, may now significantly contribute by participating in a new critical subnetwork, lowering drastically k_c (in Fig. 2, for the horizontal surface, $L_{m1H} = 193\,\mu$m, whereas $L_c = 123\,\mu$m and L_{m1H}/L_c gives 1.57).

As explained before, reporting the value of L_c on the electron micrograph of Fig. 8 can illustrate what is the typical size of a critical path opening. It is also worth mentioning that L_c and $D_c = (2\sqrt{2})L_c$ provide a rather reliable rough estimate of the characterized values for Λ and Λ', respectively (see Table III). This tends to confirm the customarily assumed idea that the small openings (windows) and the pore itself (cell) are, respectively, associated to viscous and thermal dissipation effects. What could be the consequences of isotropy and fully-reticulated cells assumptions related to Eqs. (1) and (2) in the determination of the PUC sizes? (1) An elongation of a fully reticulated unit cell (obtained by an increase of the inclination angle θ) would presumably not significantly modify the critical sizes in the longitudinal direction, and, accordingly, nor the above-mentioned characterized viscous and thermal length rough estimates (only a slight reduction in the thermal length is anticipated — see Sec. V A). But a permeability reduction, to be characterized (see Sec. III D), might be anticipated in the transverse direction. (2) Ignoring membranes results in a significant artificial reduction of both r_c and L_c compared to the PUC sizes that would be obtained for an isotropic unit cell with non-fully reticulated membranes (R_1 case). In this last situation, it seems reasonable to infer the following rules of thumbs: $\Lambda \sim L_c - 2(r_c + \delta)$, where δ is taken as a typical membrane

TABLE III. Local characteristic lengths L_c and D_c of the reconstructed idealized unit cells compared to macroscopic viscous and thermal characteristic lengths Λ and Λ' for the three polyurethane foam samples R_1, R_2, and R_3. Parentheses indicate the relative difference when L_c is compared to Λ and D_c is compared to Λ'.

Characteristic lengths	Method	R_1	R_2	R_3
$L_c (\mu m)$		123	141	158
$D_c = (2\sqrt{2})L_c \ (\mu m)$		348	399	447
$\Lambda (\mu m)$	Computations	297 (−59%)	279 (−49%)	373 (−58%)
	Characterization[a]	129 (−5%)	118 (+19%)	226 (−30%)
$\Lambda' (\mu m)$	Computations	506 (−31%)	477 (−16%)	647 (−31%)
	Characterization[b]	440 (−21%)	330 (+21%)	594 (−25%)

[a]Reference 54.
[b]Reference 55.

size and $\Lambda' \leq 2(L_c\sqrt{2} - r_c)$, where the inequality would tend to a strict equality for $\delta \to 0$.

VI. ADDITIONAL JUSTIFICATION AND VALIDATION OF THE PROPOSED METHOD

What could be the microstructural characteristic lengths governing the long wavelengths' acoustic properties of real motionless foam samples? This is a question dominating the studies on the microphysical basis behind transport phenomena we addressed from critical path considerations in the present paper. In other words, why should we use the new method presented in Fig. 9(b) compared to the one presented in Fig. 9(a)? And can we really base our understanding of the foam acoustic behavior on the L_c parameter? To answer these questions and thus convince the reader to use the method presented here, a conceptual and practical justification is given, and an analysis of the uncertainties associated to L_c determination is then provided.

A. Conceptual and practical justification

The characteristic lengths governing transport and acoustic properties of real foam samples depend on the distributions of pore and window sizes. Although they might be determined from the average value of numerous cells captured with microtomography[23] (Fig. 9(a)), this would be justified only in the specific case of sharply peaked distributions[5] (when the averaged and critical lengths coincide, as in Fig. 2 R_3). Furthermore, even if the pore and window size distributions of the real porous system to be analyzed are sharply peaked, the approach presented in this paper for the analysis of transport and acoustic properties in real porous media allows circumventing microtomography techniques, which remain not

commonly available and time consuming. Our work was inspired by critical-path ideas borrowed from statistical physics.[57] For instance, critical path considerations suggest that viscous fluid transport in a real system of polyhedral open cells with a broad distribution of ligament lengths is dominated by those polyhedral cells of permeabilities greater than some critical value k_c and, thus, by their corresponding critical ligament length L_c. The critical permeability k_c represents the largest permeability, such that the set of permeabilities $\{k|k > k_c\}$ still forms an infinite, connected cluster. Hence, viscous transport in such a system reduces to a critical path problem with threshold value k_c. We thus interpreted viscous transport within foam pore spaces in terms of these critical path ideas in order to identify what could be a basic ingredient to the microstructural key linkages governing the long wavelengths' acoustic properties of real motionless foam samples (necessary but not sufficient, see Sec. V). Since the local viscous permeability is a function of the ligament length L, the threshold permeability k_c defines a critical length L_c, which is a length that was identified from measurements of the viscous permeability k_0 over a real foam sample. Moreover, the length that marks the permeability threshold in the critical viscous permeability problem also defines the threshold in the experimental viscous permeability case (see Appendix A). This means that, in general, L_c for the viscous permeability is different from the averaged ligament
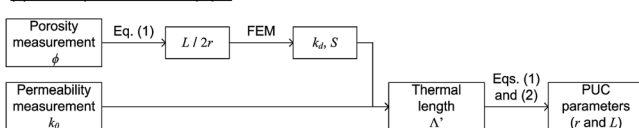

FIG. 9. Schematic comparison between two different methods leading to the periodic unit cell parameters (PUC) expressed as: (a) the average ligament lengths L_m and thicknesses $2r_m$ or, alternatively, (b) the ligament lengths L and thicknesses $2r$ governing the permeability k_0 of the real foam sample under study and interpreted in terms of critical characteristic lengths.
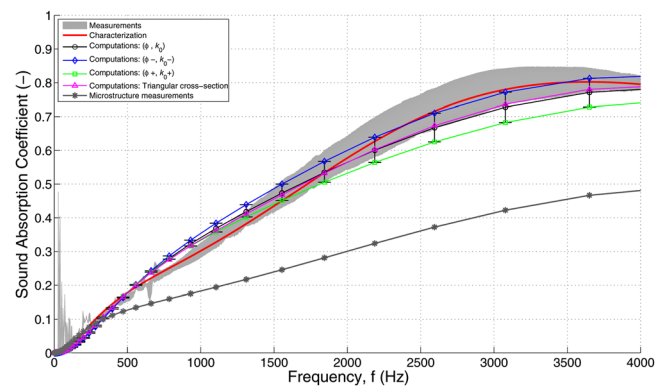

FIG. 10. (Color online) Normal incidence sound absorption coefficient for foam sample R_1. Comparison between measurements (Ref. 32), characterization (Refs. 54 and 55 combined with models described in Appendix B), and computations (this work). Adding to the model experimental uncertainties for k_0 and ϕ helps improve the correspondence between experiments and modeling. Direct microstructure measurements are also used as input parameters of the three-dimensional local geometry model. The triangular cross-section shapes local model does not significantly modify the overall sound absorbing behavior. Sample thickness: 25 mm.
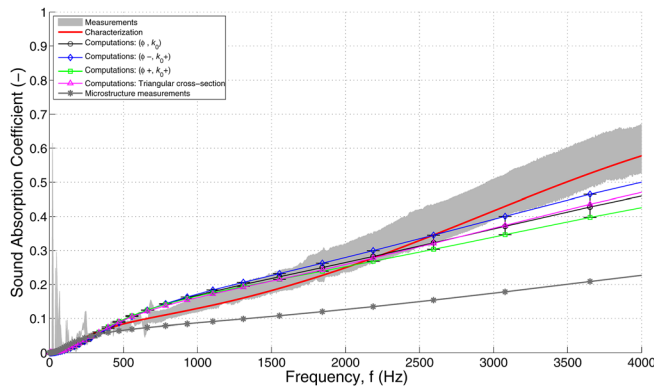
FIG. 11. (Color online) Normal incidence sound absorption coefficient for foam sample R_2. Comparison between measurements (Ref. 32), characterization (Refs. 54 and 55 combined with models described in Appendix B), and computations (this work). Adding to the model experimental uncertainties for k_0 and ϕ helps improve the correspondence between experiments and modeling. Direct microstructure measurements are also used as input parameters of the three-dimensional local geometry model. The triangular cross-section shapes local model does not significantly modify the overall sound absorbing behavior. Sample thickness: 15 mm.

FIG. 12. (Color online) Normal incidence sound absorption coefficient for foam sample R_3. Comparison between measurements (Ref. 32), characterization (Refs. 54 and 55 combined with models described in Appendix B), and computations (this work). Adding to the model experimental uncertainties for k_0 and ϕ helps improve the correspondence between experiments and modeling. Direct microstructure measurements are also used as input parameters of the three-dimensional local geometry model. The triangular cross-section shapes local model does not significantly modify the overall sound absorbing behavior. Sample thickness: 15 mm.

lengths L_m. In other words, the very long ligaments have an excessive weight in the computation of the predicted permeability, except if the distribution of the ligament lengths is sharply peaked, as in Fig. 2 R_3. This property is quantitatively illustrated below in Sec. VI B. We derived some general results concerning the relationship between experimental permeability k_0 and critical ligament length L_c by specifying the function $k_0 = f(L_c)$ for a given polyhedral shape. These relationships hold as long as the cellular shape of the local geometry model is compatible with real foam samples.

B. Quantitative validation through uncertainty analysis

To confirm further the correspondence between experiment and modeling, we tested the prediction that computation of the normal incidence sound absorbing behavior with the average ligament length L_m and thickness $2r_m$ as direct input parameters for the local geometry model should diminish the agreement (Figs. 10 and 11), except for a real foam sample exhibiting a rather sharply peaked ligament length distribution with isolated membranes and anisotropy (Fig. 12). Only in this last case, using directly measured ligament lengths $L_m = 157 \, (\pm 19) \, \mu$m and thicknesses $2r_m = 25 \, (\pm 10) \, \mu$m as input parameters to the local geometry model increases the agreement without any adjustable parameter (see Appendix C for the measurement procedure of the ligament thicknesses). Remark that, in the computations, the JCAPL model was used. Adding to the model experimental uncertainties for k_0 and ϕ helps improve the correspondence between experiments and modeling: R_1 (ϕ^-, k_0^-); R_2 (ϕ^-, k_0^-); and R_3 (ϕ^+, k_0^+), where subscripts − and + are used to designate the lower and upper bounds of related quantities with respect to some experimental uncertainties (0.01 for porosity, 10% of the mean measured value for permeability). Introducing concave triangular cross-section shapes with a fillet at the cusps instead of circular cross-section shapes in the model does not significantly modify the overall acousti-
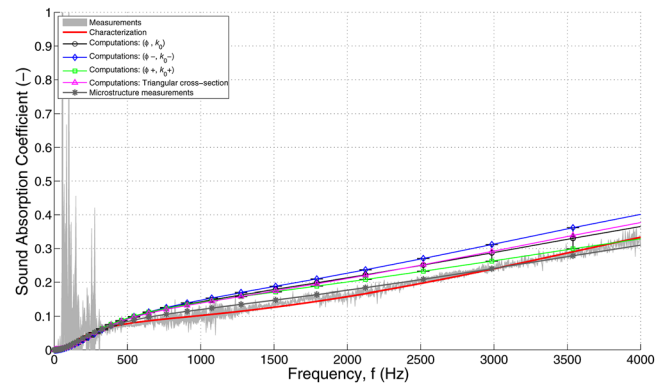
cal macro-behavior. This and the results above justify and validate the proposed method and indicate that it captures the essential physics of the asymptotic low-frequency fluid-structure interactions in a real foam sample.

VII. CONCLUSION

A three-dimensional idealized periodic unit cell (PUC)-based method to obtain the acoustic properties of three predominantly open-cell foam samples was described. The first step was to provide the local characteristic lengths of the representative unit cell. For isotropic open cell foams, two input parameters were required: the porosity and the static viscous (hydraulic) permeability. Long wavelengths' acoustic properties were derived from the three-dimensional reconstructed PUC by solving the boundary value problems governing the micro-scale propagation and visco-thermal dissipation phenomena with adequate periodic boundary conditions and further field phase averaging. The computed acoustic properties of the foams were found to be in relatively good agreement with standing wave tube measurements. A close examination of the real foam sample ligament length distribution as observed from micrographs and its comparison with the characteristic size of the local geometry model showed evidences of membrane and cellular anisotropy effects discussed by means of critical path considerations. In summary, we have developed a microcellular approach in which the local characteristic length L_c governing the static viscous permeability of a real foam sample can be identified and from which rough estimates of the viscous Λ and thermal lengths Λ' may follow (small openings and pore size itself). The overall picture that emerges from that work is that the acoustical response of these materials is governed by their three-dimensional micro-cellular morphology, for which an idealized unit-cell based method is a convenient framework of multi-scale analysis displaying the microgeometry features having a significant impact on the overall response function of the porous media.

The deviations between numerical and experimental results in the high frequency range were related to membrane and anisotropy effects, which were not taken into account by a simple three-dimensional non-elongated and open-cell geometry model. It will be the subject of a forthcoming work. Indeed, it was shown through preliminary simulations that the deviations were therefore significantly reduced when the three-dimensional unit-cell was allowed to present membranes at the peripheral of its windows and forced to follow the elongation of the real foam sample as measured from microscopy. This confirms the validity of the proposed approach and indicates that it captures the essential physics of the fluid-structure interactions in a real foam sample. In a forthcoming paper, it will be shown that the predictions of transport parameters and long-wavelength acoustical macro-behavior are in excellent agreement with measurements for three-dimensional, membrane-based, elongated local geometry models exhibiting the essential features of real foam sample microstructures having a significant impact at the upper scale.

APPENDIX A: CRITICAL PATH CONSIDERATIONS

The purpose of this appendix is to present how a "critical path argument" can be used for helping to estimate the characteristic dimensions of a three-dimensional unit-cell, which can represent, at the best, the physics occurring through a real foam sample having macro-scale static viscous permeability k_0. Following Ambegaokar, Halperin, and Langer[5,57] for the explanation of the hopping conductivity in disordered semiconductors, it is useful to think, for our purpose, of a real foam sample as a network of randomly distributed unit-cells with a broad distribution of ligament lengths L and having polyhedral shapes linked between two sites i and j by local permeabilities $\tilde{k}_{ij}$. In general, any unit-cell in the network will be connected by an appreciably large permeability only to its close neighbors, and the discussion of the possible applicability of a simple three-dimensional unit-cell to model the overall static viscous permeability k_0 of a real foam sample involves the relations between a set of such sites. Obviously, the geometry does not correspond to a percolation threshold, but some features of random media used in percolation studies can be of use here. In this picture, the correct choice for the characteristic unit-cell corresponds to the critical permeability k_c, such that the subset of unit-cells with $k_{ij} > k_c$ still contains a connected network, which spans the entire sample. Since the local viscous permeability is a function of the length L, the threshold permeability k_c defines a characteristic length L_c.

The reasoning behind this statement is as follows. A real foam sample can be considered as composed of three parts:

(i)   A set of isolated regions of high permeability, each region consisting of a group of unit-cells with long ligament lengths and permeabilities $k_{ij} \gg k_c$.

(ii)   A relatively small number of resistive unit-cells with k_{ij} of order k_c and ligament lengths of order L_c, which connect together a subset of the high permeability clusters to form an infinite network, which spans the system. The set of unit-cells in categories (i) and (ii) is the critical subnetwork.

(iii)   The remaining unit-cells with $k_{ij} \ll k_c$ and $L \ll L_c$.

The permeabilities in category (i) and their corresponding ligament lengths could all be set equal to infinity without greatly affecting the total permeability — the permeability would still be finite, because the flow has to pass through unit-cells with permeabilities of order k_c and ligament lengths of order L_c to get from one end of the sample to the other. On the other end, the unit-cells with $k_{ij} \ll k_c$ and $L \ll L_c$ make a negligible contribution to the permeability, because they are effectively shorted out by the critical subnetwork of unit-cells with $k_{ij} \geq k_c$ and $L \geq L_c$. It is now clear that the unit-cells with permeabilities of order k_c and ligament lengths of order L_c determine the permeability of the real foam sample k_0, i.e., $k_c = k_0$ and $L = L_c$.

In contrast, the choice of a length in the neighborhood of the averaged ligament lengths L_m would alter the value of the predicted permeability from the exaggerated contribution of the very large ligaments and would not be directly relevant to the representative unit-cell for the viscous flow.

APPENDIX B: DIFFERENT LEVELS IN MODELING THE ACOUSTICS OF POROUS MEDIA

To describe the macro-scale acoustic properties of rigid-frame, air-saturated porous media, the knowledge of two complex (~) response factors are required. The dynamic tortuosity $\tilde{\alpha}_{ij}(\omega)$ is defined by analogy with the response of an ideal (non-viscous) fluid, for which α_{ij} is real-valued and frequency independent,

$$\rho_0 \tilde{\alpha}_{ij}(\omega) \frac{\partial \langle v_j \rangle}{\partial t} = -G_j. \tag{B1}$$

$\tilde{\alpha}_{ij}(\omega) = \tilde{\rho}_{ij}(\omega)/\rho_0$ is related to the dynamic viscous permeability by $\tilde{\alpha}_{ij}(\omega) = \nu\phi/i\omega\tilde{k}_{ij}(\omega)$. In these expressions, $\tilde{\rho}_{ij}(\omega)$ is the effective density of air in the pores, ρ_0 is the density of air at rest, and $\nu = \eta/\rho_0$ is the air kinematic viscosity.

Similarly, a compressibility effect is also observed at macro-scale in the acoustic response of a thermo-conducting, fluid-filled porous media, where a second convenient response factor is the normalized dynamic compressibility $\tilde{\beta}(\omega)$, which varies from the isothermal to the adiabatic value when frequency increases,

$$\frac{\tilde{\beta}(\omega)}{K_a}\frac{\partial \langle p \rangle}{\partial t} = -\mathbf{\nabla} \cdot \langle \mathbf{v} \rangle. \tag{B2}$$

Here, $\tilde{\beta}(\omega) = K_a/\tilde{K}(\omega)$ is directly related to the dynamic (scalar) thermal permeability[28] by means of the relation $\tilde{\beta}(\omega) = \gamma - (\gamma - 1)i\omega\tilde{k}'(\omega)/\nu'\phi$. In these equations, $\tilde{K}(\omega)$ is the effective dynamic bulk modulus of air in the pores, $K_a = \gamma P_0$ is the air adiabatic bulk modulus, P_0 the atmospheric pressure, $\gamma = C_p/C_v$ is the specific heat ratio at constant temperature, $\nu' = \kappa/\rho_0 C_p$, and C_p and C_v are the specific heat capacity at constant pressure and volume.

With a locally plane interface, having no fractal character, the long wavelength frequency dependence of the visco-thermal response factors $\tilde{\alpha}_{ij}(\omega)$ and $\tilde{\beta}(\omega)$ have to respect definite and relatively universal behaviors[4,47,53] (namely causality through the Kramers-Kronig relation), similarly to models used for relaxation phenomena in dielectric properties. The equivalent dynamic tortuosity of the material and the equivalent dynamic compressibility of the material are $\tilde{\alpha}_{eqij}(\omega) = \tilde{\alpha}_{ij}(\omega)/\phi$ and $\tilde{\beta}_{eq}(\omega) = \phi\tilde{\beta}(\omega)$.

Simple analytic admissible functions for the fluid phase effective properties for *isotropic* porous media, respecting the causality conditions, are

$$\tilde{\alpha}(\omega) = \alpha_\infty\left[1 + \frac{1}{i\varpi}f(\varpi)\right],$$

$$\tilde{\beta}(\omega) = \gamma - (\gamma - 1)\left[1 - \frac{1}{i\varpi'}f'(\varpi')\right]^{-1}, \tag{B3}$$

where $\tilde{f}$ and $\tilde{f}'$ are form functions defined by

$$\tilde{f}(\varpi) = 1 - P + P\sqrt{1 + \frac{M}{2P^2}i\varpi},$$

$$\tilde{f}'(\varpi') = 1 - P' + P'\sqrt{1 + \frac{M'}{2P'^2}i\varpi'}, \tag{B4}$$

and ϖ and ϖ' are dimensionless viscous and thermal angular frequencies given by the following expressions:

$$\varpi = \frac{\omega}{\nu}\frac{k_0\alpha_\infty}{\phi}, \quad \varpi' = \frac{\omega}{\nu'}\frac{k_0'}{\phi}. \tag{B5}$$

The quantities M, M', P, and P' are dimensionless shape factors,

$$M = \frac{8k_0\alpha_\infty}{\Lambda^2\phi}, \quad M' = \frac{8k_0'}{\Lambda'^2\phi}, \quad P = \frac{M}{4\left(\frac{\alpha_0}{\alpha_\infty} - 1\right)},$$

$$P' = \frac{M'}{4(\alpha_0' - 1)}. \tag{B6}$$

- For $M' = P = P' = 1$ (with the requirement that $k_0' \approx \phi\Lambda'^2/8$), the dynamic visco-inertial and thermal response functions reduce to 5 parameters (ϕ, k_0, α_∞, Λ, Λ') named throughout the paper as "Johnson-Champoux-Allard" [JCA] model
- When the requirement $k_0' \approx \phi\Lambda'^2/8$ is not fulfilled, k_0' must be explicitly taken into account; this is the 6 parameters "Johnson-Champoux-Allard-Lafarge" [JCAL] model, where M' may differ from unity
- A complete model relies on 8 parameters (ϕ, k_0, k_0', α_∞, Λ, Λ', α_0, and α_0') and correctly matches the frequency dependence of the first two leading terms of the exact result for both high and low frequencies. This is the refined "Johnson-Champoux-Allard-Pride-Lafarge" [JCAPL] model.

Looking for plane waves solutions varying as $\exp[i(\omega t - \tilde{q}x)]$, Eqs. (B1) and (B2) yield the equivalent dynamic wave number $\tilde{q}_{eq}(\omega)$ of the material and equivalent characteristic impedance $\tilde{Z}_{eq}(\omega)$ of the material,

$$\tilde{q}_{eq} = \omega\left(\tilde{\alpha}_{eq}(\omega)\tilde{\beta}_{eq}(\omega)\frac{\rho_0}{K_a}\right)^{\frac{1}{2}}, \quad \tilde{Z}_{eq} = \left(\frac{\tilde{\alpha}_{eq}(\omega)}{\tilde{\beta}_{eq}(\omega)}\rho_0 K_a\right)^{\frac{1}{2}}. \tag{B7}$$

Thus, $\tilde{\alpha}_{eq}(\omega)$ and $\tilde{\beta}_{eq}(\omega)$ provide all pertinent information on the propagation and dissipation phenomena in the equivalent homogeneous material. Assuming an absorbing porous layer of thickness L_s that is backed by a rigid wall, the normal incidence sound absorption coefficient is

$$A_n = 1 - \left|\frac{\tilde{Z}_{sn} - 1}{\tilde{Z}_{sn} + 1}\right|^2, \tag{B8}$$

with the normalized surface impedance of the porous medium defined as

$$\tilde{Z}_{sn} = \frac{\tilde{Z}_{eq}}{\rho_0 c_0}\coth(i\tilde{q}_{eq}L_s), \tag{B9}$$

where c_0 is the sound speed in air.

APPENDIX C: LIGAMENT THICKNESSES MEASUREMENT PROCEDURE

An estimation of the ligament thicknesses was provided through complementary measurements on SEM. Ligament thickness measurements were performed on two perpendicular cross-sections of each foam sample on the basis of 10 SEM for each perpendicular cross-section. These pictures were obtained with an environmental scanning electron microscope (ESEM), Electroscan E3 available at Laboratoire Géomatériaux et Environnement from Université Paris-Est, using an accelerating voltage of 20 or 30 kV with a lanthanum hexaboride (LaB$_6$) cathodes electron source. Using a typical magnification, spanning from ×150 to ×200, measurements were carried out at the center of the ligaments (at the midpoint between two nodes). Note that the light zone situated at the peripheral of the ligaments and attributed to

membranes was deliberately ignored during measurements. This is consistent with typical dimensions of observable transverse cross-sections. For each foam sample, the average ligament thickness estimates yield: R_1, $2r_{m1} = 31 \pm 7\,\mu m$ ($2r_1 = 19 \pm 7\,\mu m$); R_2, $2r_{m2} = 36 \pm 8\,\mu m$ ($2r_2 = 27 \pm 7\,\mu m$); and R_3, $2r_{m3} = 30 \pm 6\,\mu m$ ($2r_3 = 25 \pm 10\,\mu m$). Note that there is a reasonable agreement between computed and measured ligament thickness estimates, accounting for standard deviations.

[1]J. W. S. Rayleigh, *The Theory of Sound*, 2nd ed. (Dover, New York, 1945).
[2]C. Zwikker and C. W. Kosten, *Sound Absorbing Materials* (Elsevier, Amsterdam, 1949).
[3]J. F. Allard and N. Atalla, *Propagation of Sound in Porous Media: Modeling Sound Absorbing Materials*, 2nd ed. (Wiley, Chichester, 2009).
[4]D. L. Johnson, J. Koplik, and R. Dashen, J. Fluid Mech. **176**, 379 (1987).
[5]M. Y. Zhou and P. Sheng, Phys. Rev. B **39**, 12027 (1989).
[6]I. Malinouskaya, V. V. Mourzenko, J.-F. Thovert, and P. M. Adler, Phys. Rev. E **77**, 066302 (2008). C. Peyrega, "*Prediction of the acoustic properties of heterogeneous fibrous materials from their 3D microstructures*," Ph.D. dissertation (Mines ParisTech, 2010).
[7]A. Cortis and J. G. Berryman, Phys. Fluids **22**, 053603 (2010).
[8]C. Boutin and C. Geindreau, J. Acoust. Soc. Am. **124**, 3576 (2008).
[9]C. Boutin and C. Geindreau, Phys. Rev. E **82**, 036313 (2010).
[10]T. Lévy, Int. J. Eng. Sci. **17**, 1005 (1979).
[11]J. L. Auriault, Int. J. Eng. Sci. **18**, 775 (1980).
[12]J. L. Auriault, L. Borne, and R. Chambon, J. Acoust. Soc. Am. **77**, 1641 (1985).
[13]R. Burridge and J. B. Keller, J. Acoust. Soc. Am. **70**, 1140 (1981).
[14]C. Boutin and J. L. Auriault, Int. J. Eng. Sci. **28**, 1157 (1990).
[15]L. J. Gibson and M. F. Ashby, *Cellular Solids: Structure and Properties* (Cambridge University Press, Cambridge, 1988).
[16]D. Weaire and S. Hutzler, *The Physics of Foams* (Oxford University Press, Oxford, 1999).
[17]M. R. Stinson, J. Acoust. Soc. Am. **89**, 550 (1991).
[18]P. M. Adler, *Porous Media: Geometry and Transports* (Butterworth-Heinemann, Stoneham, 1992).
[19]K. Attenborough, J. Acoust. Soc. Am. **73**, 785 (1983).
[20]S. Gasser, F. Paun, and Y. Brechet, J. Acoust. Soc. Am. **117**(4I), 2090 (2005).
[21]C.-Y. Lee, M. J. Leamy, and J. H. Nadler, J. Acoust. Soc. Am. **126**, 1862 (2009).
[22]K. Schladitz, S. Peters, D. Reinel-Bitzer, A. Wiegmann, and J. Ohser, Comput. Mater. Sci. **38**, 56 (2006).
[23]C. Perrot, R. Panneton, and X. Olny, J. Appl. Phys. **101**, 113538 (2007).
[24]C. Perrot, R. Panneton, and X. Olny, J. Appl. Phys. **102**, 074917 (2007).
[25]C. Perrot, F. Chevillotte, and R. Panneton, J. Appl. Phys. **103**, 024909 (2008).
[26]F. Chevillotte, C. Perrot, and R. Panneton, J. Acoust. Soc. Am. **128**(4) 1766 (2010).
[27]C. Perrot, F. Chevillotte, and R. Panneton, J. Acoust. Soc. Am. **124**, 940 (2008).
[28]D. Lafarge, P. Lemarinier, J. F. Allard, and V. Tarnow, J. Acoust. Soc. Am. **102**, 1995 (1997).
[29]S. R. Pride, F. D. Morgan, and A. F. Gangi, Phys. Rev. B **47**, 4964 (1993).
[30]D. Lafarge, "*Propagation du son dans les matériaux poreux à structure rigide saturés par un fluide viscothermique*," (translation in English: "*Sound propagation in rigid porous media saturated by a viscothermal fluid*"), Ph. D. dissertation, (Université du Maine, 1993).
[31]D. Lafarge, "The equivalent fluid model," in *Materials and Acoustics Handbook*, edited by C. Potel and M. Bruneau (Wiley, Chichester, 2009), Chap. 6, Part II, pp. 167–201.
[32]H. Utsuno, T. Tanaka, T. Fujikawa, and A. F. Seybert, J. Acoust. Soc. Am. **86**, 637 (1989).
[33]E. B. Matzke, Am. J. Bot. **33**, 58 (1946).
[34]A. M. Kraynik, D. A. Reinelt, and F. van Swol, Phys. Rev. Lett. **93**, 208301 (2004).
[35]L. L. Beranek, J. Acoust. Soc. Am. **13**, 248 (1942).
[36]M. R. Stinson and G. A. Daigle, J. Acoust. Soc. Am. **83**, 2422 (1988).
[37]E. N. Schmierer, A. Razani, J. W. Paquette, and K. J. Kim, in *Proceedings of 2004 ASME Heat Transfer/Fluids Engineering Summer Conference* (ASME, Charlotte, North Carolina, 2004), p. 229.
[38]A. Bhattacharya, V. V. Calmidi, and R. L. Mahajan, Int. J. Heat Mass Transfer **45**, 1017 (2002).
[39]M. Firdaouss, J.-L. Guermond, and D. Lafarge, Int. J. Eng. Sci. **36**, 1035 (1998).
[40]Y. Achdou and M. Avellaneda, Phys. Fluids A **4**, 2651 (1992).
[41]Y. Champoux and J. F. Allard, J. Appl. Phys. **70**, 1975 (1991).
[42]S. Brunauer, P. H. Emmett, and E. Teller, J. Am. Chem. Soc. **60**, 309 (1938).
[43]M. Henry, P. Lemarinier, J. F. Allard, J. L. Bonardet, and A. Gedeon, J. Appl. Phys. **77**, 17 (1994).
[44]J. Rouquerol, D. Avnir, C. W. Fairbridge, D. H. Everett, J. M. Haynes, N. Pernicone, J. D. F. Ramsay, K. S. W. Sing, and K. K. Unger, Pure Appl. Chem. **66**, 1739 (1994).
[45]J.-L. Auriault, C. Boutin, and C. Geindreau, *Homogenization of Coupled Phenomena in Heterogeneous Media* (Wiley-ISTE, London, UK, 2009).
[46]R. J. S. Brown, Geophysics **45**, 1269 (1980).
[47]M. Avellaneda and S. Torquato, Phys. Fluids A **3**, 2529 (1991).
[48]A. Cortis, D. M. J. Smeulders, J. L. Guermond, and D. Lafarge, Phys. Fluids **15**, 1766 (2003).
[49]J. Rubinstein and S. Torquato, J. Chem. Phys. **88**, 6372 (1988).
[50]P. Göransson, R. Gustavino, and N.-E. Hörlin, J. Sound Vib. **327**, 354 (2009).
[51]C. Perrot, F. Chevillotte, R. Panneton, J.-F. Allard, and D. Lafarge, J. Acoust. Soc. Am. **124**, EL210 (2008).
[52]N. Martys and E. J. Garboczi, Phys. Rev. B **46**, 6080 (1992).
[53]D. Lafarge, Phys. Fluids A **5**, 500 (1993).
[54]R. Panneton and X. Olny, J. Acoust. Soc. Am. **119**, 2027 (2006).
[55]X. Olny and R. Panneton, J. Acoust. Soc. Am. **123**, 814 (2008).
[56]R. M. Sullivan, L. J. Ghosn, and B. A. Lerch, Int. J. Solids Struct. **45**, 1754 (2008).
[57]V. Ambegaokar, B. I. Halperin, and J. S. Langer, Phys. Rev. B **4**, 2612 (1971).